LANGMUIR Article
Cite This: Langmuir 2018, 34, 4554−4559
pubs.acs.org/Langmuir

Correlation between Gas Bubble Formation and Hydrogen Evolution Reaction Kinetics at Nanoelectrodes

Qianjin Chen[†,‡] and Long Luo*[,†]

[†]Department of Chemistry, Wayne State University, Detroit, Michigan 48202, United States
[‡]College of Chemistry, Chemical Engineering and Biotechnology, Donghua University, Shanghai 201620, China

Supporting Information

ABSTRACT: We report the correlation between H_2 gas bubble formation potential and hydrogen evolution reaction (HER) activity for Au and Pt nanodisk electrodes (NEs). Microkinetic models were formulated to obtain the HER kinetic information for individual Au and Pt NEs. We found that the rate-determining steps for the HER at Au and Pt NEs were the Volmer step and the Heyrovsky step, respectively. More interestingly, the standard rate constant (k^0) of the rate-determining step was found to vary over 2 orders of magnitude for the same type of NEs. The observed variations indicate the HER activity heterogeneity at the nanoscale. Furthermore, we discovered a linear relationship between bubble formation potential (E_{bubble}) and log(k^0) with a slope of 125 mV/decade for both Au and Pt NEs. As log (k^0) increases, E_{bubble} shifts linearly to more positive potentials, meaning NEs with higher HER activities form H_2 bubbles at less negative potentials. Our theoretical model suggests that such linear relationship is caused by the similar critical bubble formation condition for Au and Pt NEs with varied sizes. Our results have potential implications for using gas bubble formation to evaluate the HER activity distribution of nanoparticles in an ensemble.

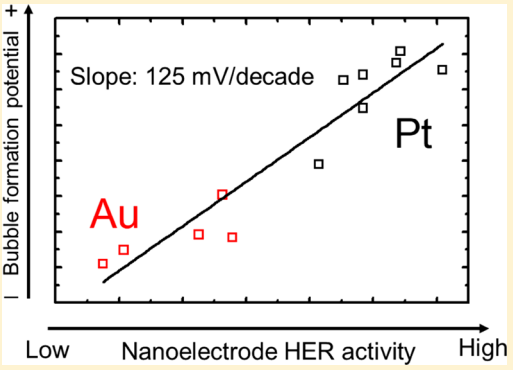

INTRODUCTION

Discovery of electrocatalytic nanoparticles (NPs) for water splitting reactions, the oxygen evolution reaction (OER) and hydrogen evolution reaction (HER), have received increasing attention.[1−6] One effective strategy for NP catalysts development is to understand the structure−activity relationship and then use the findings to guide the catalyst design. The most common approach for correlating the structure and reactivity of NPs is to devise good synthetic methods for preparing uniform NPs, characterize the resulting ensemble, and compare the reactivities of different ensembles as a function of a structural variation, such as NP size.[7−9] The limitation of this approach arises from the technical challenges in synthesizing uniform NPs. Efforts to circumvent this limitation have been made by shifting to individual NP studies where uniform NPs are not the prerequisite.[10−14] However, such studies have their own challenges. One key challenge is the lack of high-throughput methods for characterizing electrocatalytic activities of individual NPs. Our proposal to efficiently evaluate the HER and OER activities of individual NPs is to image the bubble formation resulting from the gas-evolving reaction at a single NP. This approach is based on the hypothesis that the potential for gas bubble formation at a NP will be related to its catalytic activity for gas generation.

Several methods have been previously developed to detect and characterize interfacial nanobubbles, such as tapping-mode atomic force microscopy,[15,16] optical microscopy,[17,18] and electrochemistry.[19−26] To test our hypothesis, we use nanoelectrodes (NEs) to represent individual NPs because of their similar sizes and electrocatalytic activity and to study the correlation between bubble formation and the HER kinetics. Specifically, Pt and Au nanodisk electrodes with radii less than 50 nm were prepared and used to perform the HER in 1.0 M $HClO_4$ (see Experimental Section and Figures S1, S2 for the NE fabrication method). Pt and Au were chosen to test the general applicability of our hypothesis because of their dramatically different HER activities.[2,27] A typical cyclic voltammogram for a Pt NE is shown in Figure 1. As the electrode potential is scanned negative of ∼−0.2 V vs Ag/AgCl (the thermodynamic potential for H^+/H_2),[28] the current increases rapidly until it reaches a peak value at ∼−0.4 V. The current drop corresponds to the nucleation and formation of a gas bubble at the NE, which in turn blocks the electrode surface.[20,23,24] The potential where the current drops is denoted as E_{bubble}. The standard rate constant of the rate-determining step for the HER at a NE, k^0, was obtained by conducting microkinetic analyses of the current prior to the bubble formation. Gas bubble formation potential was then correlated with the HER activities by comparing E_{bubble} and k^0. We found a linear relationship between E_{bubble} and log(k^0) with a slope of 125 mV/decade confirming that the potential for H_2 bubble formation at a NE is related to its HER activity. More

Received: February 7, 2018
Revised: March 21, 2018
Published: March 23, 2018

DOI: 10.1021/acs.langmuir.8b00435
Langmuir 2018, 34, 4554−4559

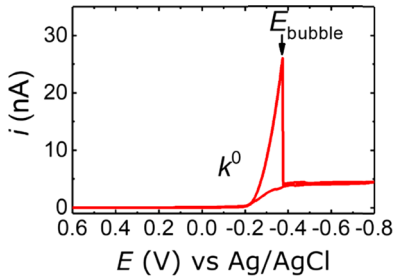

Figure 1. Cyclic voltammogram for a 34 nm radius Pt NE in N_2-purged 1.0 M $HClO_4$. The potential was cycled between 0.6 and −0.8 V vs Ag/AgCl at a scan rate of 100.0 mV/s. The current drop at ∼−0.4 V (defined as E_{bubble}) corresponds to the nucleation and formation of a gas bubble at the electrode surface. The standard rate constant of the rate-determining step, k^0, is obtained by conducting a microkinetic analysis of the current prior to the bubble formation.

interestingly, both Pt and Au NEs follow the same trend line although they have different HER mechanisms and activities suggesting the relationship is not limited to one metal. After combining theoretical models and experimental results, we have elucidated that the linear relationship arises from the similar critical condition for H_2 bubble nucleation for Pt and Au. The findings above have confirmed our hypothesis and imply the potential use of H_2 bubble formation for evaluating the HER activities of individual Pt or Au monometallic NPs and Pt/Au bimetallic NPs.

EXPERIMENTAL SECTION

Materials. Perchloric acid ($HClO_4$, 70%), sodium perchlorate ($NaClO_4$, 98%), calcium chloride ($CaCl_2$, 99%), ferrocene (Fc, 98%), and tetrabutylammonium hexafluorophosphate ($TBAPF_6$) were all purchased from Sigma-Aldrich. Glass capillary (o.d./i.d., 1.65/0.75 mm, soft temperature, 700 °C) was received from Dagan Corporation. Platinum (Pt wire, 25 μm diameter, 99.95%) and gold (Au wire, 25 μm diameter, 99.95%) wires were purchased from Alfa Aesar. All of the aqueous solutions were prepared from deionized water (Milli-Q, 18.2 MΩ cm).

Nanoelectrode Fabrication Method. Pt and Au nanoelectrodes were fabricated as previously reported.[29] The scheme for the fabrication method is illustrated in Figure S1. The end of a 25 μm Pt or Au wire was sharpened in a 15 wt % $CaCl_2$ solution, and the representative scanning electron microscopy images are presented in Figure S2. All of the tips are very sharp with radii of curvature of ∼25 nm. After thermal sealing, a nanodisk was exposed by mechanical polishing on fine sandpaper, followed by thorough rinsing with ultrapure water.

Electrochemistry. All of the experiments were carried out using a CHI 760E potentiostat. A Ag/AgCl electrode in a saturated KCl solution was used as the counter/reference electrode during the measurements with nanoelectrodes. In all of the $HClO_4$ solutions, 0.10 M $NaClO_4$ was added as the supporting electrolyte. The apparent electrochemical radius, r, was determined by the diffusion-limited current for proton reduction (i_{lim}) in 0.10 M $HClO_4$ solution containing 0.10 M $NaClO_4$. r was calculated using $i_{lim} = 4FDCr$. D for H^+ in the solution was calibrated to be 7.8×10^{-5} cm^2/s using the same method with a 12.5 μm radius Pt ultramicroelectrode. Figure S3 shows the typical voltammograms for Pt and Au NEs with varying radii in 0.10 M H^+ solution. The radii estimated using this method are within 10% difference from the ones determined from ferrocene oxidation.

Data Fitting with Nonlinear Regression. The data fitting was carried out using the nlinfit() function in MATLAB R2017b. Prior to data fitting, the experimentally measured current was postprocessed to j_{et} (the current density that flows under the kinetic limitation) using eq 7 in the Results and Discussion. The obtained .txt data file consists of two columns of data. The first column is the electrode potential using Ag/AgCl as the reference electrode and the second column is j_{et}. The MATLAB codes for fitting the data files are provided in the Supporting Information. In the case of the Volmer step being the rate-determining step, the currentVolmer.m file defines the current expression and the FitVolmer.m file contains the nonlinear regression script. Place both files in the current folder for MATLAB and run the script in the FitVolmer.m file. In the case of the Heyrovsky step being the rate-determining step, the currentHeyrovsky.m and the FitHeyrovsky.m files were used.

RESULTS AND DISCUSSION

Microkinetic Analyses. To conduct microkinetic analyses, we first identify the correct HER kinetic models for Au and Pt NEs. Conventionally, the HER mechanism is considered to consist of two possible steps: the Volmer step and the Heyrovsky or Tafel step, as follows.[30−32]

$$\text{Volmer step: } H^+ + e^- + M \rightleftharpoons M - H \quad (1)$$

$$\text{Heyrovsky step: } H^+ + e^- + M - H \rightleftharpoons M + H_2 \quad (2)$$

$$\text{Tafel step: } 2M - H \rightleftharpoons 2M + H_2 \quad (3)$$

where M denotes the surface empty site. Each step can determine the overall rate, and their corresponding kinetic current expressions can be expressed as[33]

$$i_{et} = nFAk^0 a_{H^+} \exp(-\alpha f\eta) \quad (4)$$

$$i_{et} = nFA\frac{k^0 K^0 a_{H^+}^2 \exp(-\alpha f\eta)}{\exp(f\eta) + K^0 a_{H^+}} \quad (5)$$

$$i_{et} = nFAk^0\left[\frac{K^0 a_{H^+}^2}{\exp(f\eta) + K^0 a_{H^+}}\right]^2 \quad (6)$$

where i_{et} is the current that flows under the kinetic limitation, n is the number of electrons transferred per formation of a H_2 molecule ($n = 2$), a_{H^+} is the proton activity (approximately equal to the proton concentration, C_{H^+}), A is the electrode surface area, α is the transfer coefficient of the rate-determining step, f is equal to F/RT (F: the Faraday's constant, R: the universal gas constant, and T: the absolute temperature), η is the overpotential, and K^0 is the equilibrium constant for the Volmer step. The three rate-determining cases described above were used to fit experimental data. The correct kinetic models were identified by finding the best agreement between the experimental data and the fits.

Prior to the data fitting, the experimentally measured overall current, i, was converted to i_{et} by subtracting the contribution of the mass transfer using eq 7 analogous to the Koutecký−Levich equation in rotating disk electrode voltammetry.[28,34]

$$\frac{1}{i_{et}} = \frac{1}{i} - \frac{1}{i_{mt}} = \frac{1}{i} - \frac{1}{4FD_{H^+}C_{H^+}r} \quad (7)$$

where i_{mt} is the limiting current controlled solely by mass transfer of H^+, D_{H^+} is the diffusion coefficient of H^+ in solution (7.8×10^{-5} cm^2/s), and r is the radius of a NE that was electrochemically measured (see Figure S3). The i_{et}−E curves of Pt NEs were analyzed with a nonlinear regression method (see Experimental section for data fitting details). In the regression analyses, the values of α, K^0, and k^0 were varied to achieve the best fits. After testing all three rate-determining cases, we found that the good fits were obtained when eq 5 was used to fit the voltammograms for Pt NEs (Figure 2a). It means

DOI: 10.1021/acs.langmuir.8b00435
Langmuir 2018, 34, 4554−4559

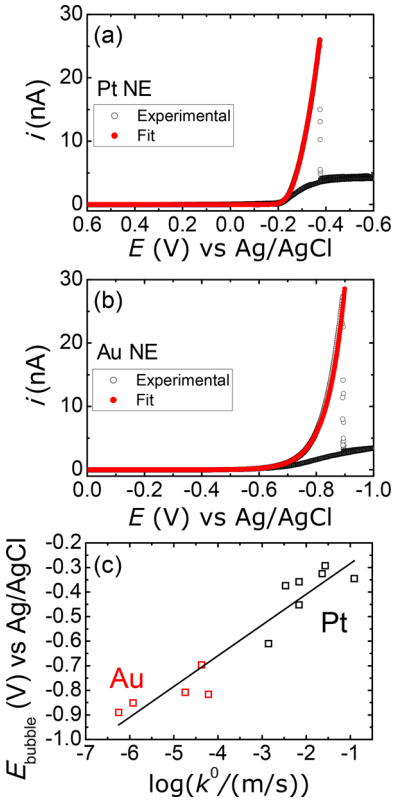

Figure 2. Experimental cyclic voltammograms (black) and their corresponding best fits (red) for a (a) 34 nm radius Pt NE and (b) 20 nm radius Au NE. Experimental conditions are the same as those used in Figure 1. The fit in (a) was obtained using eq 5, which assumes the Heyrovsky step is the rate-determining step. For this Pt NE, kinetics parameters: $\alpha = 0.40$, $K^0 = 9.8 \times 10^{-2}$ M^{-1}, and $k^0 = 0.0034$ m/s. The fit in (b) was obtained using eq 4, which assumes the Volmer step is the rate-determining step. For this Au NE, the obtained kinetics parameters are $\alpha = 0.44$ and $k^0 = 1.2 \times 10^{-6}$ m/s. (c) E_{bubble} vs $\log(k^0)$ plot for seven Pt (black square) and five Au (red square) NEs. All of the electrodes are independently prepared and tested following the same protocol. The red line is the best linear fit of the data points, which has a slope of 125 mV/decade.

that the Heyrovsky step is the rate-determining step for the HER catalyzed by Pt NEs. This finding is consistent with the HER mechanism on Pt(111) and Pt(100) in acidic solutions.[35] More quantitatively, α is calculated to be 0.5 ± 0.2 (the uncertainty is the standard deviation from seven different Pt NEs, Table 1) indicating the symmetric energy barrier for the Heyrovsky step. Because the Heyrovsky step determines the rate, the Volmer step is equilibrated prior to the Heyrovsky step. K^0 is calculated to be $(6 \pm 3) \times 10^{-2}$ M^{-1} (Table 1). The surface coverage of adsorbed H on Pt NEs, θ, is a function of K^0 expressed as[33]

$$\theta = \frac{K^0 a_{H^+}}{\exp(f\eta) + K^0 a_{H^+}} \quad (8)$$

At E_{bubble}, θ is estimated to be 0.9 ± 0.2 (Table 1 and Figure S4) indicating nearly full coverage of adsorbed H on the Pt NEs when a H_2 bubble forms. Relative to α, K^0, and θ, k^0 shows larger variations among different electrodes (from 1.4×10^{-3} to 1.2×10^{-1} m/s, Table 1). Such variation in k^0 indicates that the Pt NEs have different HER activities even though they were prepared using the same method and catalyze the HER via the same mechanism (the Heyrovsky step being rate-determining).

Table 1. HER Kinetic Parameters (K^0, k^0, and α) Obtained from Data Fitting, Bubble Formation Potentials (E_{bubble}), NE Radii, and Surface Coverage of Adsorbed H (θ) at E_{bubble} for Seven Pt NEs

Pt NE radius (nm)	K^0 (M^{-1})	k^0 (m/s)	α	E_{bubble} (V) vs Ag/AgCl	θ at E_{bubble}
11	4.7×10^{-2}	6.9×10^{-3}	0.37	−0.358	0.96
2	7.0×10^{-2}	1.2×10^{-1}	0.43	−0.345	0.95
13	3.1×10^{-2}	6.9×10^{-3}	0.32	−0.452	1.00
6	3.0×10^{-2}	2.3×10^{-2}	0.67	−0.325	0.80
20	7.8×10^{-2}	1.4×10^{-3}	0.31	−0.610	1.00
34	9.8×10^{-2}	3.4×10^{-3}	0.40	−0.374	0.99
4	3.9×10^{-2}	2.7×10^{-2}	0.97	−0.293	0.60
average	6×10^{-2}		0.5	−0.4	0.9
standard deviation	3×10^{-2}		0.2	0.1	0.2

The activity heterogeneity is not simply a size effect because two NEs with comparable sizes exhibited significantly different E_{bubble} (by ~200 mV, Figure S5). It might arise from the structural dispersion that has often been found at the nanoscale, such as nanosized grains with different crystal orientations on a polycrystalline metal surface.[36−39]

Similar nonlinear regression analyses were carried out for Au NEs. Unlike Pt NEs, good fits for Au NEs were achieved when the Volmer step was considered as the rate-determining step. In the case of the Volmer step being rate-determining, k^0 and α are the fitting parameters (refer to eq 4). Figure 2b is an example showing the great agreement between the experimental data and the numerical fit. To further validate this mechanism, we carried out a proton-concentration-dependence study. According to eq 4, there should be a first-order dependence of i on C_{H^+} at constant potentials if the HER kinetics is limited by the Volmer step. Figure S6 shows the linear relationship between $\log(i)$ and $\log(C_{H^+})$ at $E = -0.7$, -0.75, and -0.8 V with an average slope of 0.94, which is consistent with our expectation. Similar to Pt NEs, α was found to be 0.41 ± 0.05 (Table 2),

Table 2. HER Kinetic Parameters (k^0 and α) Obtained from Data Fitting, Bubble Formation Potentials (E_{bubble}), and NE Radii for Five Au NEs

Au NE radius (nm)	k^0 (m/s)	α	E_{bubble} (V) vs Ag/AgCl
20	1.2×10^{-6}	0.44	−0.851
9	6.1×10^{-5}	0.36	−0.816
19	1.8×10^{-5}	0.37	−0.808
8	4.3×10^{-5}	0.47	−0.696
34	5.6×10^{-7}	0.41	−0.890
average		0.41	
standard deviation		0.05	

which is close to 0.5, meaning the energy barrier of the Volmer step for Au NEs is also symmetric. Moreover, Au NEs exhibit significant variations in k^0 (from 5.6×10^{-7} to 6.1×10^{-5} m/s) as well. This result shows that the HER activity heterogeneity of the Pt and Au NEs is independent of the catalytic material type and the HER mechanism.

Following the extraction of the kinetic parameters from the voltammograms, E_{bubble} is plotted against k^0 for Pt and Au NEs. Figure 2c shows that E_{bubble} is linearly related with $\log(k^0)$ with a slope of 125 mV/decade. NEs with a higher HER activity (or a larger k^0) form a H_2 bubble at more positive potentials than those with a lower HER activity. It is intuitive to think of this

DOI: 10.1021/acs.langmuir.8b00435
Langmuir 2018, 34, 4554−4559

conclusion because H_2 is generated at a high rate when more active NEs are used for the HER leading to H_2 bubbles nucleation at more positive potentials. However, it is surprising to find the same linear relationship for both Pt and Au NEs because their different surface energies, including the metal/gas and metal/liquid interfacial energies, are expected to affect the gas bubble nucleation considering heterogeneous nucleation.[40,41]

Bubble Nucleation Conditions at Pt and Au NEs. To understand the linear relationship between E_{bubble} and $\log(k^0)$, we studied the bubble formation conditions at Pt and Au NEs. As previously reported,[20] the nucleation of a H_2 bubble at a Pt NE requires a supersaturation of dissolved H_2 at the NE surface. The supersaturation level can be calculated from the peak current in the voltammogram for the NEs in acid (Figures 1 and 2). Figure 3a shows the peak current (i_{peak}) as a function

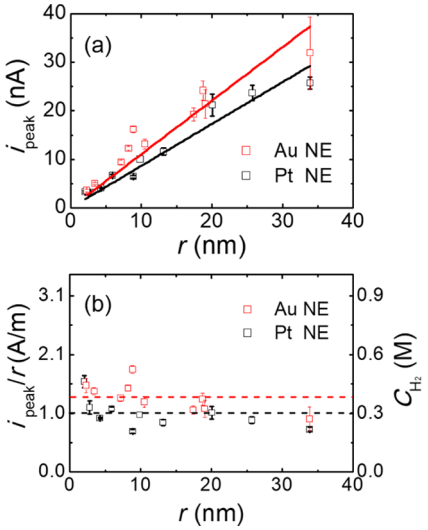

Figure 3. (a) Peak current of the cyclic voltammograms for Au (red) and Pt NEs (black) in 1.0 M $HClO_4$ (scan rate = 100.0 mV/s) as a function of NE radii. Error bars are from at least three measurements using the same electrode. The lines are the best fits of the data points. (b) The concentration of dissolved H_2 at the NE surface that is required for bubble nucleation and formation, C_{H_2}, as a function of NE radii. The dashed lines are the average values of the data points.

of electrode radii (r) for Au and Pt NEs. The error bars represent the standard deviations from at least three independent measurements using the same electrode. For both Au and Pt NEs, the peak current varies linearly with radii. The slope for Au NEs (1.1 ± 0.1 A/m) is similar to that for Pt NEs (0.9 ± 0.1 A/m). Because i_{peak} arises from the reduction of H^+, the steady-state dissolved H_2 concentration at the electrode surface (C_{H_2}) can be estimated from the peak current using the following expression[28]

$$i_{peak} = 4nFD_{H_2}C_{H_2}r \tag{9}$$

where D_{H_2} is the diffusivity of H_2 (4.5×10^{-5} cm^2/s).[42] Figure 3b shows a relatively constant C_{H_2} for the H_2 bubble nucleation at Au or Pt NEs having varying radii. It means the critical concentration of dissolved H_2 that is required for bubble nucleation and formation at NEs is independent of electrode size. The average C_{H_2} values for Au (red dashed line) and Pt (black dashed line) are estimated to be two similar values: 0.38 ± 0.07 and 0.30 ± 0.07 M, respectively. This finding is significant because it shows that the bubble nucleation condition is not sensitive to the HER activity of NEs (k^0 varies from ~10^{-6} to 10^{-1} m/s for Au and Pt NEs in Figure 2c). Note that the C_{H_2} for Pt NEs measured in this study is slightly larger than the value previously reported (0.25 M) using the same experimental conditions except that the solution was 0.5 M H_2SO_4.[24] Despite the differences, these two values are very close considering the experimental error.

Linear Relationship between E_{bubble} and $\log(k^0)$. On the basis of the analyses described above, we continued to investigate the linear relationship between E_{bubble} and $\log(k^0)$ by deriving the numerical expression of E_{bubble} for Au and Pt NEs. As previously concluded, the rate-determining step for the HER at Au NEs is the Volmer step and eq 4 is the expression for the electrokinetic current. At E_{bubble}, eq 4 can be rewritten as eq 10.

$$\frac{1}{\left(\frac{1}{4nFD_{H_2}C_{H_2}r} - \frac{1}{4FD_{H^+}C_{H^+}r}\right)} = nFAk^0C_{H^+}\exp(-\alpha f E_{bubble}) \tag{10}$$

This equation can be rearranged to the expression for E_{bubble}

$$E_{bubble} = \frac{1}{\alpha f \log e}\log(k^0) + \frac{1}{\alpha f}\ln(r) + \frac{1}{\alpha f}\ln\left[nF\pi C_{H^+}\left(\frac{1}{4nFD_{H_2}C_{H_2}} - \frac{1}{4FD_{H^+}C_{H^+}}\right)\right] \tag{11}$$

The third term in eq 11 can be treated as a constant because C_{H_2} is constant for different Au NEs (~0.38 M) at E_{bubble} (the critical condition for bubble nucleation and formation). Thus, we see that E_{bubble} is linearly correlated with the $\log(k^0)$ with a slope of $\frac{1}{\alpha f \log e}$ or 118 mV/decade if r is constant, which is very close to our measured 125 mV/decade in Figure 2c. For Pt NEs, the rate-determining step is the Heyrovsky step governed by eq 5. At E_{bubble}, however, eq 5 can also be simplified to eq 4 because $\exp(f\eta)$ in the denominator of eq 5 is ~100 times smaller than the other term of the denominator: $K^0a_{H^+}$ (the average values of η and K^0 were measured to be −0.2 V and 6×10^{-2} M^{-1}, respectively). Therefore, the relationship between E_{bubble} and $\log(k^0)$ for Pt NEs becomes identical to that for Au NEs leading to the linear relationship in Figure 2c.

The linear relationship between E_{bubble} and $\log(k^0)$ for NEs is generally valid when the electrode size variation is within ~3-fold. Figure 4a shows the contour plot for E_{bubble} as a function of $\log(k^0)$ and r for Au and Pt NEs, which is described by eq 11. E_{bubble} moves from ~−0.9 to ~−0.3 V as $\log(k^0)$ increases from 10^{-7} to 10^{-1} in great agreement with the experimental result (Figure 2c). In addition, E_{bubble} also exhibits a slightly positive shift of ~60 mV at a fixed $\log(k^0)$ as r increases from 10 to 30 nm (Figure 4b). However, the E_{bubble} shift due to the size effect is less significant than that observed in experiment (up to ~300 mV, Table 1) further confirming that the different E_{bubble} is mainly caused by the different HER activities among NEs.

■ CONCLUSIONS

In conclusion, we have shown that the bubble formation potential at NEs is related to their HER activity at Au and Pt NEs. As the HER activity increases, bubble formation potential shifts to more positive potentials. We began the study with the

DOI: 10.1021/acs.langmuir.8b00435
Langmuir 2018, 34, 4554−4559

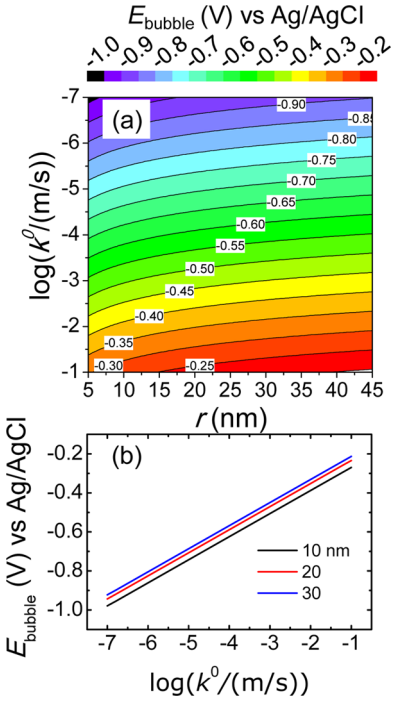

Figure 4. (a) Contour plot of E_{bubble} as a function of $\log(k^0)$ and r for Au and Pt NEs, which is governed by eq 11. (b) E_{bubble} vs $\log(k^0)$ plots for NEs with r = 10, 20, and 30 nm. The slopes for the three lines are identical: 118 mV/decade.

microkinetic analyses of the voltammetric responses for NEs. The results show that the rate-determining steps for the HER at Au and Pt NEs are the Volmer step and the Heyrovsky step, respectively. The measured kinetic rate constants of the rate-determining step were found to vary over 2 orders of magnitude for the same type of NEs. The observed HER activity variations are likely to arise from the structural heterogeneity among NEs. We also found that different NEs exhibited a similar critical condition for bubble formation (~300−400 folds supersaturation of dissolved H_2 at the NE surface) even though the HER activities largely vary among these NEs. Furthermore, we discovered a linear relationship between bubble formation potential (E_{bubble}) and $\log(k^0)$, which was explained by our theoretical models. Both Au and Pt NEs having different radii follow the same trend line suggesting this relationship is insensitive to the size and the HER mechanism. Our findings in this work provide a valuable fundamental insight into the relationship between bubble formation potential and the HER activity for NEs. Because of the similar sizes and electrocatalytic activities between NEs and NPs, our findings could guide the development of a bubble-based method that uses the bubble formation potential as the criterion for rapidly and conveniently evaluating the HER activity distribution on a catalytic surface or in an ensemble of catalytic NPs.

■ ASSOCIATED CONTENT

Supporting Information

The Supporting Information is available free of charge on the ACS Publications website at DOI: 10.1021/acs.langmuir.8b00435.

Nanoelectrode fabrication procedures, data fitting scripts, voltammograms for NE sizing, estimated coverage of adsorbed H for Pt NEs, and perchloric acid concentration dependence study for Au NEs (PDF)

■ AUTHOR INFORMATION

Corresponding Author

*E-mail: long.luo@wayne.edu (L.L.).

ORCID

Long Luo: 0000-0001-5771-6892

Notes

The authors declare no competing financial interest.

■ ACKNOWLEDGMENTS

This work was supported by the start-up funds and Ebbing Faculty Development Award from Wayne State University. We thank Dr. Zhiyao Duan (the University of Texas at Austin) and Dr. H. Bernhard Schlegel (Wayne State University) for helpful discussions. L.L. thanks Dr. Stephanie Brock (Wayne State University) for proofreading the manuscript.

■ REFERENCES

(1) Popczun, E. J.; Read, C. G.; Roske, C. W.; Lewis, N. S.; Schaak, R. E. Highly Active Electrocatalysis of the Hydrogen Evolution Reaction by Cobalt Phosphide Nanoparticles. *Angew. Chem.* **2014**, *126*, 5531−5534.

(2) Jaramillo, T. F.; Jørgensen, K. P.; Bonde, J.; Nielsen, J. H.; Horch, S.; Chorkendorff, I. Identification of Active Edge Sites for Electrochemical H_2 Evolution from MoS_2 Nanocatalysts. *Science* **2007**, *317*, 100−102.

(3) Gong, M.; Zhou, W.; Tsai, M.-C.; Zhou, J.; Guan, M.; Lin, M.-C.; Zhang, B.; Hu, Y.; Wang, D.-Y.; Yang, J.; et al. Nanoscale Nickel Oxide/Nickel Heterostructures for Active Hydrogen Evolution Electrocatalysis. *Nat. Commun.* **2014**, *5*, No. 4695.

(4) Voiry, D.; Yamaguchi, H.; Li, J.; Silva, R.; Alves, D. C.; Fujita, T.; Chen, M.; Asefa, T.; Shenoy, V. B.; Eda, G.; et al. Enhanced Catalytic Activity in Strained Chemically Exfoliated WS_2 Nanosheets for Hydrogen Evolution. *Nat. Mater.* **2013**, *12*, 850.

(5) Liang, Y.; Li, Y.; Wang, H.; Zhou, J.; Wang, J.; Regier, T.; Dai, H. Co_3O_4 Nanocrystals on Graphene as a Synergistic Catalyst for Oxygen Reduction Reaction. *Nat. Mater.* **2011**, *10*, 780−786.

(6) Wang, H.; Lee, H.-W.; Deng, Y.; Lu, Z.; Hsu, P.-C.; Liu, Y.; Lin, D.; Cui, Y. Bifunctional Non-Noble Metal Oxide Nanoparticle Electrocatalysts through Lithium-Induced Conversion for Overall Water Splitting. *Nat. Commun.* **2015**, *6*, No. 7261.

(7) Kinoshita, K. Particle Size Effects for Oxygen Reduction on Highly Dispersed Platinum in Acid Electrolytes. *J. Electrochem. Soc.* **1990**, *137*, 845−848.

(8) Mayrhofer, K. J. J.; Blizanac, B.; Arenz, M.; Stamenkovic, V.; Ross, P.; Markovic, N. The Impact of Geometric and Surface Electronic Properties of Pt-Catalysts on the Particle Size Effect in Electrocatalysis. *J. Phys. Chem. B* **2005**, *109*, 14433−14440.

(9) Wang, Y.-J.; Zhao, N.; Fang, B.; Li, H.; Bi, X. T.; Wang, H. Carbon-Supported Pt-Based Alloy Electrocatalysts for the Oxygen Reduction Reaction in Polymer Electrolyte Membrane Fuel Cells: Particle Size, Shape, and Composition Manipulation and Their Impact to Activity. *Chem. Rev.* **2015**, *115*, 3433−3467.

(10) Lai, S. C. S.; Dudin, P. V.; Macpherson, J. V.; Unwin, P. R. Visualizing Zeptomole (Electro)Catalysis at Single Nanoparticles within an Ensemble. *J. Am. Chem. Soc.* **2011**, *133*, 10744−10747.

(11) Xiao, X.; Fan, F.-R. F.; Zhou, J.; Bard, A. J. Current Transients in Single Nanoparticle Collision Events. *J. Am. Chem. Soc.* **2008**, *130*, 16669−16677.

(12) Li, Y.; Cox, J. T.; Zhang, B. Electrochemical Responses and Electrocatalysis at Single Au Nanoparticles. *J. Am. Chem. Soc.* **2010**, *132*, 3047−3054.

DOI: 10.1021/acs.langmuir.8b00435
Langmuir 2018, 34, 4554−4559

(13) Anderson, T. J.; Zhang, B. Single-Nanoparticle Electrochemistry through Immobilization and Collision. *Acc. Chem. Res.* **2016**, *49*, 2625−2631.
(14) Sambur, J. B.; Chen, P. Approaches to Single-Nanoparticle Catalysis. *Annu. Rev. Phys. Chem.* **2014**, *65*, 395−422.
(15) Lou, S.-T.; Ouyang, Z.-Q.; Zhang, Y.; Li, X.-J.; Hu, J.; Li, M.-Q.; Yang, F.-J. Nanobubbles on Solid Surface Imaged by Atomic Force Microscopy. *J. Vac. Sci. Technol., B: Nanotechnol. Microelectron.: Mater., Process., Meas., Phenom.* **2000**, *18*, 2573−2575.
(16) Zhang, X. H.; Maeda, N.; Craig, V. S. Physical Properties of Nanobubbles on Hydrophobic Surfaces in Water and Aqueous Solutions. *Langmuir* **2006**, *22*, 5025−5035.
(17) Karpitschka, S.; Dietrich, E.; Seddon, J. R. T.; Zandvliet, H. J. W.; Lohse, D.; Riegler, H. Nonintrusive Optical Visualization of Surface Nanobubbles. *Phys. Rev. Lett.* **2012**, *109*, No. 066102.
(18) Su, H.; Fang, Y.; Chen, F.; Wang, W. Monitoring Dynamic Photocatalytic Activity of Single Cds Nanoparticles by Lighting up H_2 Nanobubbles with Fluorescent Dyes. *Chem. Sci.* **2018**, 1448−1453.
(19) Ren, H.; German, S. R.; Edwards, M. A.; Chen, Q.; White, H. S. Electrochemical Generation of Individual O_2 Nanobubbles Via H_2O_2 Oxidation. *J. Phys. Chem. Lett.* **2017**, *8*, 2450−2454.
(20) Luo, L.; White, H. S. Electrogeneration of Single Nanobubbles at Sub-50-nm-Radius Platinum Nanodisk Electrodes. *Langmuir* **2013**, *29*, 11169−11175.
(21) German, S. R.; Edwards, M. A.; Ren, H.; White, H. S. Critical Nuclei Size, Rate, and Activation Energy of H_2 Gas Nucleation. *J. Am. Chem. Soc.* **2018**, 4047−4053.
(22) Chen, Q.; Wiedenroth, H. S.; German, S. R.; White, H. S. Electrochemical Nucleation of Stable N_2 Nanobubbles at Pt Nanoelectrodes. *J. Am. Chem. Soc.* **2015**, *137*, 12064−12069.
(23) Chen, Q.; Luo, L.; White, H. S. Electrochemical Generation of a Hydrogen Bubble at a Recessed Platinum Nanopore Electrode. *Langmuir* **2015**, *31*, 4573−4581.
(24) Chen, Q.; Luo, L.; Faraji, H.; Feldberg, S. W.; White, H. S. Electrochemical Measurements of Single H_2 Nanobubble Nucleation and Stability at Pt Nanoelectrodes. *J. Phys. Chem. Lett.* **2014**, *5*, 3539−3544.
(25) Gao, R.; Ying, Y.-L.; Hu, Y.-X.; Li, Y.-J.; Long, Y.-T. Wireless Bipolar Nanopore Electrode for Single Small Molecule Detection. *Anal. Chem.* **2017**, *89*, 7382−7387.
(26) Gao, R.; Lin, Y.; Ying, Y. L.; Liu, X. Y.; Shi, X.; Hu, Y. X.; Long, Y. T.; Tian, H. Dynamic Self-Assembly of Homogenous Microcyclic Structures Controlled by a Silver-Coated Nanopore. *Small* **2017**, *13*. 10.1002/smll.201700234.
(27) Greeley, J.; Jaramillo, T. F.; Bonde, J.; Chorkendorff, I.; Nørskov, J. K. Computational High-Throughput Screening of Electrocatalytic Materials for Hydrogen Evolution. *Nat. Mater.* **2006**, *5*, 909−913.
(28) Bard, A. J.; Faulkner, L. R.; Leddy, J.; Zoski, C. G. *Electrochemical Methods: Fundamentals and Applications*; Wiley: New York, 1980.
(29) Zhang, B.; Galusha, J.; Shiozawa, P. G.; Wang, G.; Bergren, A. J.; Jones, R. M.; White, R. J.; Ervin, E. N.; Cauley, C. C.; White, H. S. Bench-Top Method for Fabricating Glass-Sealed Nanodisk Electrodes, Glass Nanopore Electrodes, and Glass Nanopore Membranes of Controlled Size. *Anal. Chem.* **2007**, *79*, 4778−4787.
(30) Sheng, W.; Gasteiger, H. A.; Shao-Horn, Y. Hydrogen Oxidation and Evolution Reaction Kinetics on Platinum: Acid vs Alkaline Electrolytes. *J. Electrochem. Soc.* **2010**, *157*, B1529−B1536.
(31) Durst, J.; Siebel, A.; Simon, C.; Hasche, F.; Herranz, J.; Gasteiger, H. A. New Insights into the Electrochemical Hydrogen Oxidation and Evolution Reaction Mechanism. *Energy Environ. Sci.* **2014**, *7*, 2255−2260.
(32) Vetter, K. J. *Electrochemical Kinetics: Theoretical and Experimental Aspects*; Academic Press, 1967.
(33) Shinagawa, T.; Garcia-Esparza, A. T.; Takanabe, K. Insight on Tafel Slopes from a Microkinetic Analysis of Aqueous Electrocatalysis for Energy Conversion. *Sci. Rep.* **2015**, *5*, No. 13801.
(34) Hill, C. M.; Kim, J.; Bard, A. J. Electrochemistry at a Metal Nanoparticle on a Tunneling Film: A Steady-State Model of Current Densities at a Tunneling Ultramicroelectrode. *J. Am. Chem. Soc.* **2015**, 11321−11326.
(35) Marković, N. M.; Grgur, B.; Ross, P. Temperature-Dependent Hydrogen Electrochemistry on Platinum Low-Index Single-Crystal Surfaces in Acid Solutions. *J. Phys. Chem. B* **1997**, *101*, 5405−5413.
(36) Mariano, R. G.; McKelvey, K.; White, H. S.; Kanan, M. W. Selective Increase in CO_2 Electroreduction Activity at Grain-Boundary Surface Terminations. *Science* **2017**, *358*, 1187−1192.
(37) Liu, C.-M.; Lin, H.-W.; Huang, Y.-S.; Chu, Y.-C.; Chen, C.; Lyu, D.-R.; Chen, K.-N.; Tu, K.-N. Low-Temperature Direct Copper-to-Copper Bonding Enabled by Creep on (111) Surfaces of Nano-twinned Cu. *Sci. Rep.* **2015**, *5*, No. 9734.
(38) Aaronson, B. D.; Chen, C.-H.; Li, H.; Koper, M. T.; Lai, S. C.; Unwin, P. R. Pseudo-Single-Crystal Electrochemistry on Polycrystalline Electrodes: Visualizing Activity at Grains and Grain Boundaries on Platinum for the Fe^{2+}/Fe^{3+} Redox Reaction. *J. Am. Chem. Soc.* **2013**, *135*, 3873−3880.
(39) Chen, C.-H.; Meadows, K. E.; Cuharuc, A.; Lai, S. C.; Unwin, P. R. High Resolution Mapping of Oxygen Reduction Reaction Kinetics at Polycrystalline Platinum Electrodes. *Phys. Chem. Chem. Phys.* **2014**, *16*, 18545−18552.
(40) Blander, M.; Katz, J. L. Bubble Nucleation in Liquids. *AIChE J.* **1975**, *21*, 833−848.
(41) German, S. R.; Edwards, M.; Ren, H.; White, H. Critical Nuclei Size, Rate, and Activation Energy of H_2 Gas Nucleation. *J. Am. Chem. Soc.* **2018**, 4047−4053.
(42) Mazarei, A. F.; Sandall, O. C. Diffusion Coefficients for Helium, Hydrogen, and Carbon Dioxide in Water at 25 C. *AIChE J.* **1980**, *26*, 154−157.

DOI: 10.1021/acs.langmuir.8b00435
Langmuir 2018, 34, 4554−4559